Supplementary Information

Precursor-Regulated Reconstruction of Cu-based Catalysts for Efficient Electrocatalytic Urea Synthesis from CO_2 and Nitrate

Ke Wu [a], *Guojie Ye* [a], *Zhengwei Zhou* [a], *Zuofeng Chen* [b], *Zhendong Lei* [a] *and Deli Wu* [a]*.

[a] State Key Laboratory of Water Pollution Control and Green Resource Recycling, College of Environmental Science & Engineering, Key Laboratory of Water Supply, Water Saving and Ecological Governance in the Yangtze River Delta, Ministry of Water Resources, Shanghai Institute of Pollution Control and Ecological Security, Tongji University, Shanghai 200092, China.

[b] Shanghai Key Laboratory of Chemical Assessment and Sustainability, School of Chemical Science and Engineering, Tongji University, Shanghai 200092, China.

* Corresponding author:

Deli Wu

Email: wudeli@tongji.edu.cn

ORCID ID: https://orcid.org/0000-0002-8565-0779

Chemicals. Hydrophobic carbon paper (SCL-28BC) was obtained from Suzhou Sinero Technology Co., Ltd., ultrasonic washing with acetone and deionized water before use. Acetone (AR) and KNO_3 (GR) were purchased from Sinopharm Chemical Reagent Co., Ltd. KHCO3(AR, ≥99.5%,), Isopropyl alcohol (C_3H_8O, AR, ≥99.5%), Nafion perfluorinated resin solution (5wt%), N-(1-naphthyl) ethylenediamine dihydrochloride (98%), Sulfanilic acid (AR, 99.5%), NaClO (6-14% active chlorine basis), Na_2CO_3 (AR,≥99.5%), NaOH (95%, granular), salicylic acid ($C_7H_6O_3$, AR,99.5%), Sodium citrate dihydrate ($C_6H_5Na_3O_7 \cdot 2H_2O$, 99.0%) and urea (99%, biotechnology grade) were bought from Shanghai Macklin Biochemical Technology Co., Ltd. $Cu(NO_3)_2 \cdot 3H_2O$ (99%), sodium nitroferricyanide dihydrate (AR,99.0%) KNO_2 (AR,97%) were purchased from Shanghai Aladdin Biochemical Technology Co., Ltd. High-pure CO_2 (>99.999%) and Ar (>99.999%) were purchased from Shanghai Weichuang Standard Gas Analysis Technology Co., Ltd. Urease (urease activity :20KU, refined grade), produced by Shanghai Yuanye Biotechnology Co., Ltd. All chemicals were used without further purification. Deionized water (DIW) was used in all the experimental processes.

Computational Methods. The first-principle-based geometry optimization calculations were carried out within density-functional theory (DFT), implemented in the Vienna Ab Initio Simulation Package (VASP) code,[1] using the frozen-core projector augmented-wave (PAW) method to describe the interaction between the atomic cores and the valence electron density.[2] The exchange-correlation potential was approximated within the generalized gradient approximation (GGA) using the Perdew-Burke Ernzerhof (PBE) functional.[3] The dispersion corrected DFT-D3 schemes was employed to describe the Van der Waals (vdW) interactions.[4] Plane-wave cutoff energy was set to 500 eV. The conjugate gradient algorithm was used in ionic optimization, convergence threshold was set to 10-5 eV $atom^{-1}$ in electronic relaxation and 0.02 eV $Å^{-1}$ in Hellmann-Feynman force on each atom. The structure was optimized using the Monkhorst-Pack scheme for k-point sampling of the first Brillouin zone on a 2 × 2 × 1 grid.[5]

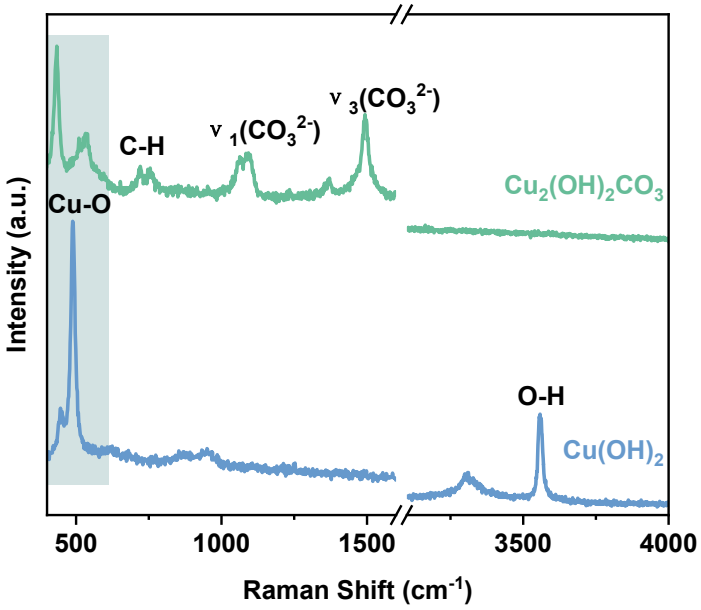

Supplementary Figure 1. FTIR spectrum of $Cu_2(OH)_2CO_3$ and $Cu(OH)_2$.

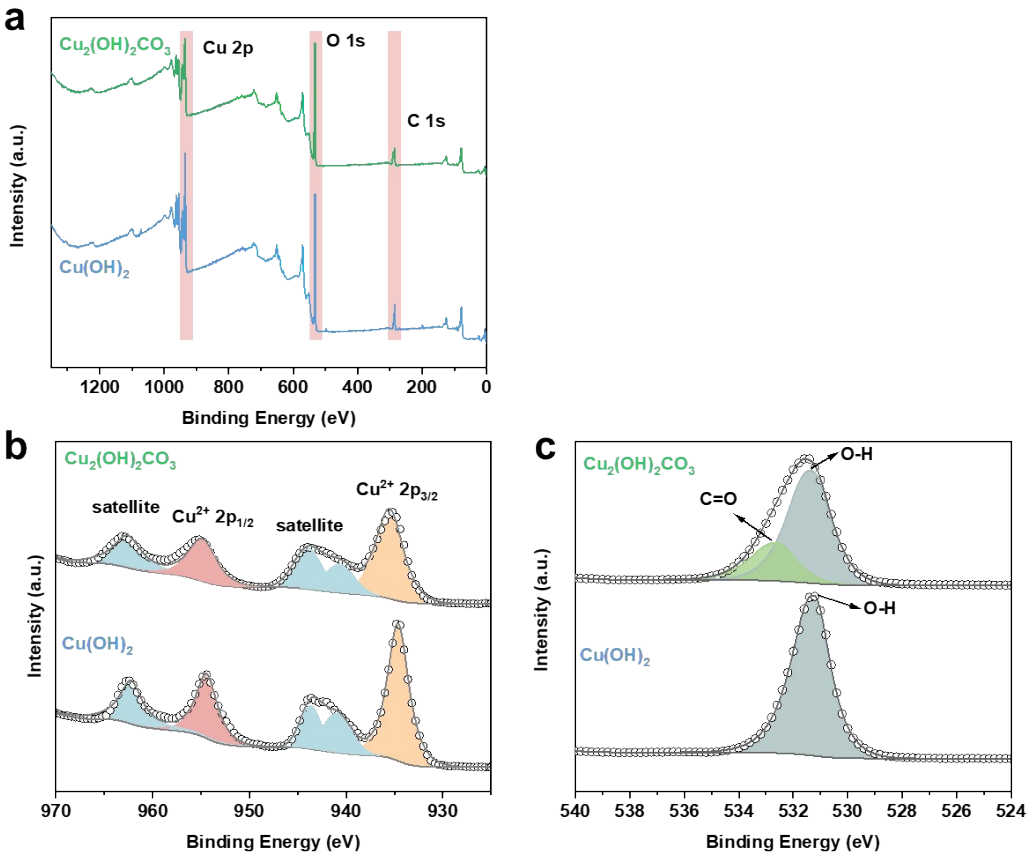

Supplementary Figure 2. a, Survey, **b,** Cu 2p, and **c,** O 1s XPS spectrum of $Cu_2(OH)_2CO_3$ and $Cu(OH)_2$.

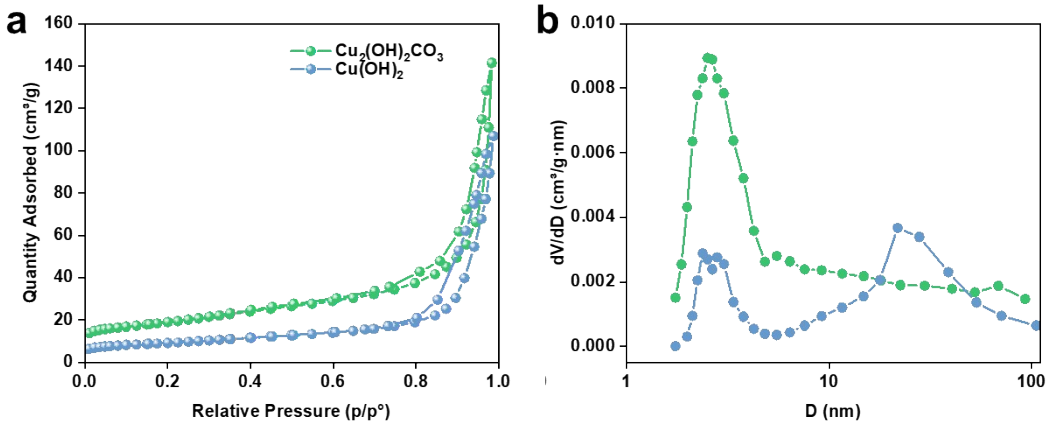

Supplementary Figure 3. a, N_2 adsorption and desorption curves, and **b,** pore size distributions of $Cu_2(OH)_2CO_3$ and $Cu(OH)_2$.

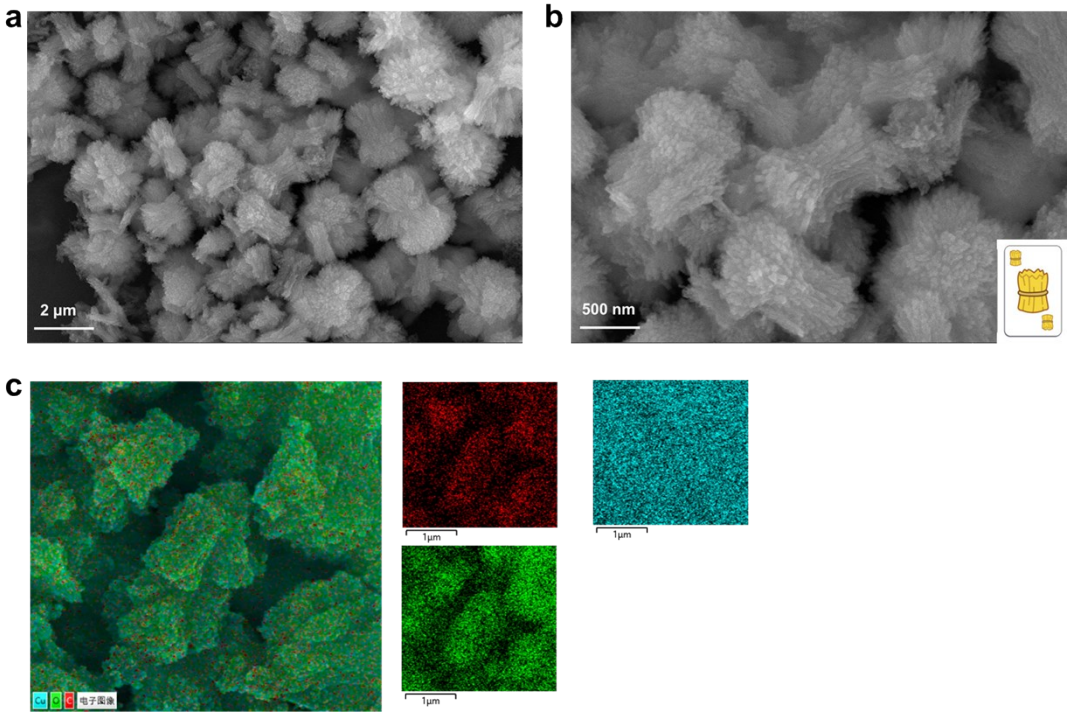

Supplementary Figure 4. SEM images of $Cu_2(OH)_2CO_3$. **a,** 2 μm, **b,** 500 nm, and **c,** corresponding EDS mapping.

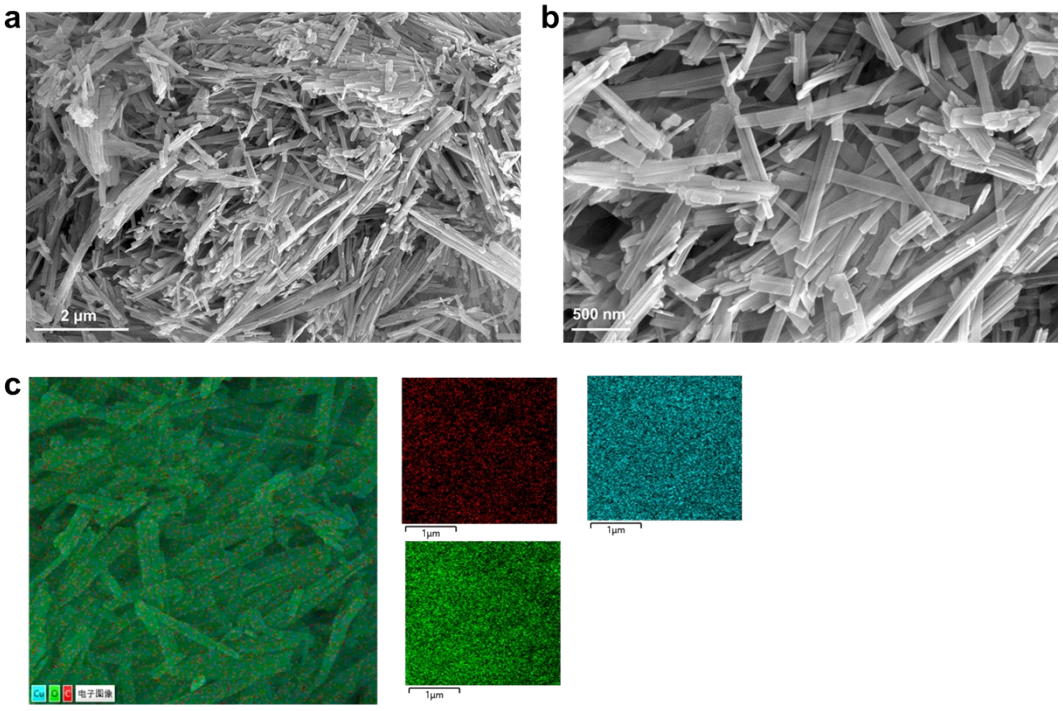

Supplementary Figure 5. SEM images of Cu(OH). **a,** 2 μm, **b,** 500 nm, and **c,** corresponding EDS mapping.

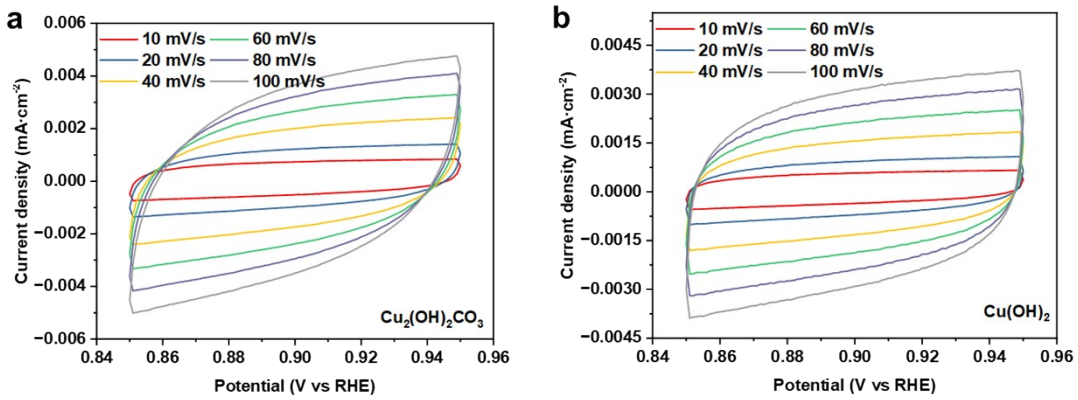

Supplementary Figure 6. The electrochemical active surface area measurements on electrocatalysts. Cyclic voltammogram curves of **a,** $Cu_2(OH)_2CO_3$, **b,** $Cu(OH)_2$.

Because electrocatalysis is in essence a surface reaction, where the adsorption/desorption of reactants/products takes place only at or near the catalyst surface region, the intrinsic electrocatalytic activity is most frequently defined as the specific activity which is the current divided by the surface area of the catalyst (e.g., mA $cm_{catalyst}^{-2}$).[6, 7] The potential window of CVs was 0.85 V to 0.95 V (vs. RHE, **Supplementary Figure 6**) in a non-Faradic potential range under different scan rates with 10, 20, 40, 60, 80 and 100 mV s^{-1}. The double layer capacitances (C_{dl}) of samples were estimated by plotting the ΔJ = Ja−Jc at 0.90 V (vs. RHE) against the scan rate. The linear slope is equivalent to twice of the double-layer capacitance C_{dl}, and the electrochemical active surface area (ECSA) of catalyst was calculated by the following equation: ECSA = C_{dl} / C_s. Where Cs is the specific capacitance of planar surface with an atomically smooth under identical electrolyte conditions, 40 μF cm^{-2} is used in this work.

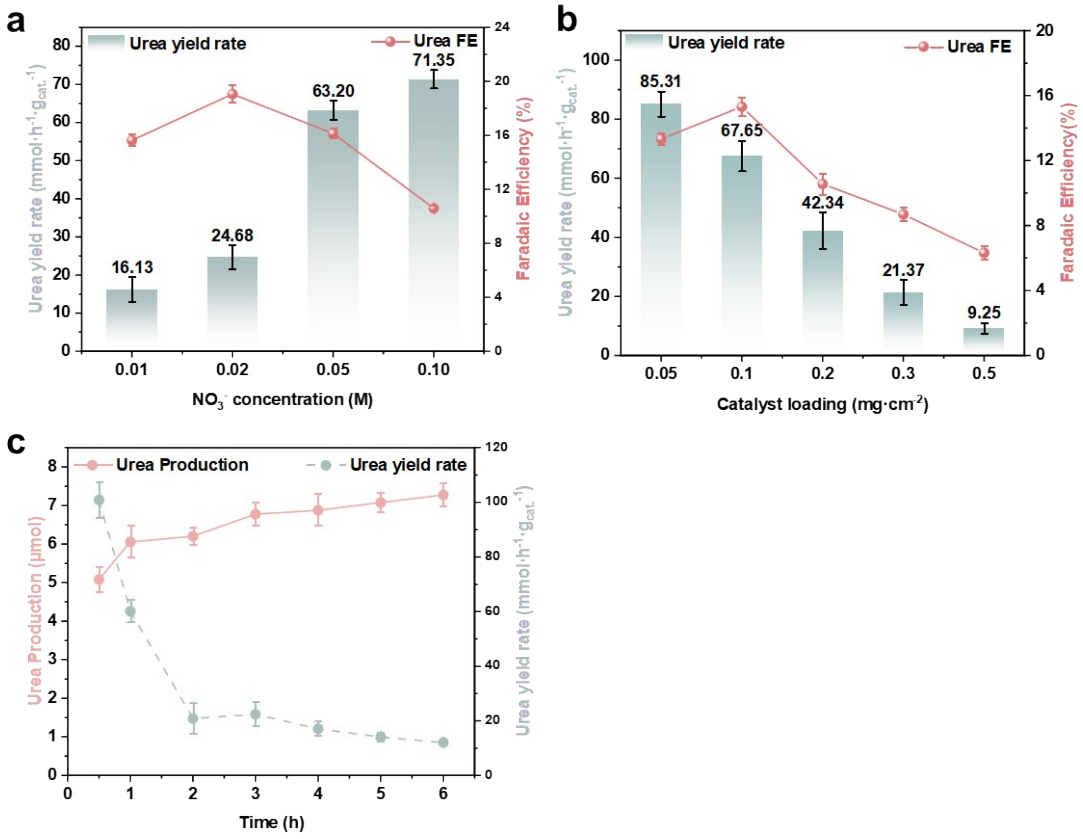

Supplementary Figure 7. Exploration of influencing factors. Urea yield rate and Faradaic Efficiency with different **a,** NO_3^- concentration, **b,** Catalyst loading, and **c,** Variation of Urea Production and Urea yield rate with electrolysis time.

The urea yield rates by coupling different concentrations of nitrate with CO_2 were depicted in **Supplementary Figure 7a**. The urea yield rates gradually increase with the nitrate concentration increased from 10 mM to 50 mM. Subsequently, the nitrate concentration continued to increase to 100 mM, the urea yield rate decreases to 3711.42 mg h^{-1} $g_{catalyst}^{-1}$. The increase of active nitrate coverage on the surface of $Cu_2(OH)_2CO_3$ catalysts promotes C–N coupling, but excessive nitrate coverage leads to the formation of by-products, which occupies too many active sites, and was not conducive to urea production. Therefore, CO_2 saturared-0.1 M $KHCO_3$ containing 0.05 M KNO_3 was

chosen as electrolyte in the subsequent experiments.

The effect of different catalyst loads on urea yield and selectivity were also investigated. As can be seen from **Supplementary Figure 7b**, with the increase of catalyst loading from 0.05 to 0.5 mg cm^{-2}, urea yield continues to decline. While urea selectivity first increases and then decreases, reaching the maximum at 0.1 mg cm^{-2}. Therefore, 0.1mg cm^{-2} was selected as the best catalyst loading capacity.

According to **Supplementary Figure 7c**, the generation of urea grew progressively during the electrolysis process and reached a maximum after ~3 h without increasing. The urea yield decreased gradually with the increase of electrolysis time. After comprehensive consideration, 1h electrolysis time was selected as the best.

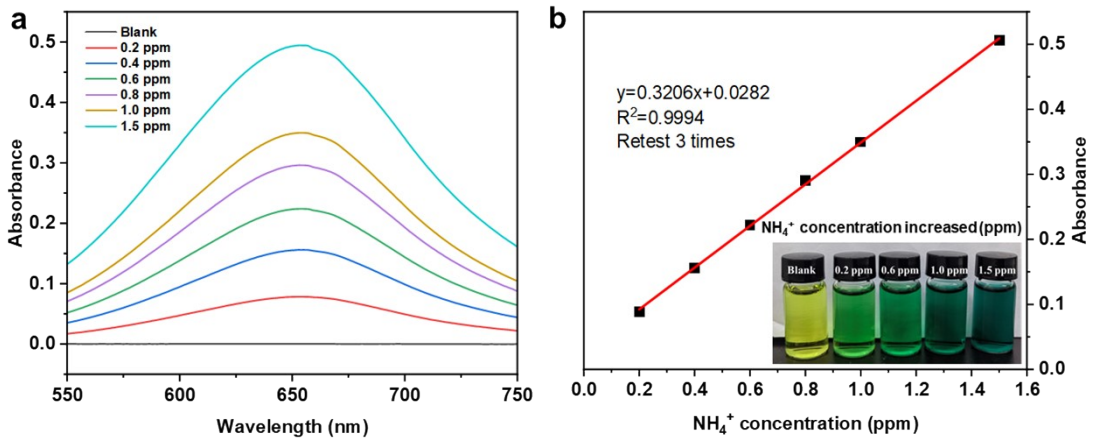

Supplementary Figure 8. Indophenol blue for NH_4^+ quantification. **a,** UV-vis absorption spectra of various NH_4^+ concentrations, and **b,** Calibration curve used for quantifying NH_4^+.

Various concentrations of NH_4^+ solutions were prepared by dissolving different qualities of NH_4Cl in mixed solutions of 0.1 M $KHCO_3$ and 0.05 M KNO_3. The concentration of NH_4^+ exhibits a linear relationship with absorbance, thus the concentration of the products could be calculated via the equation of the calibration curves.

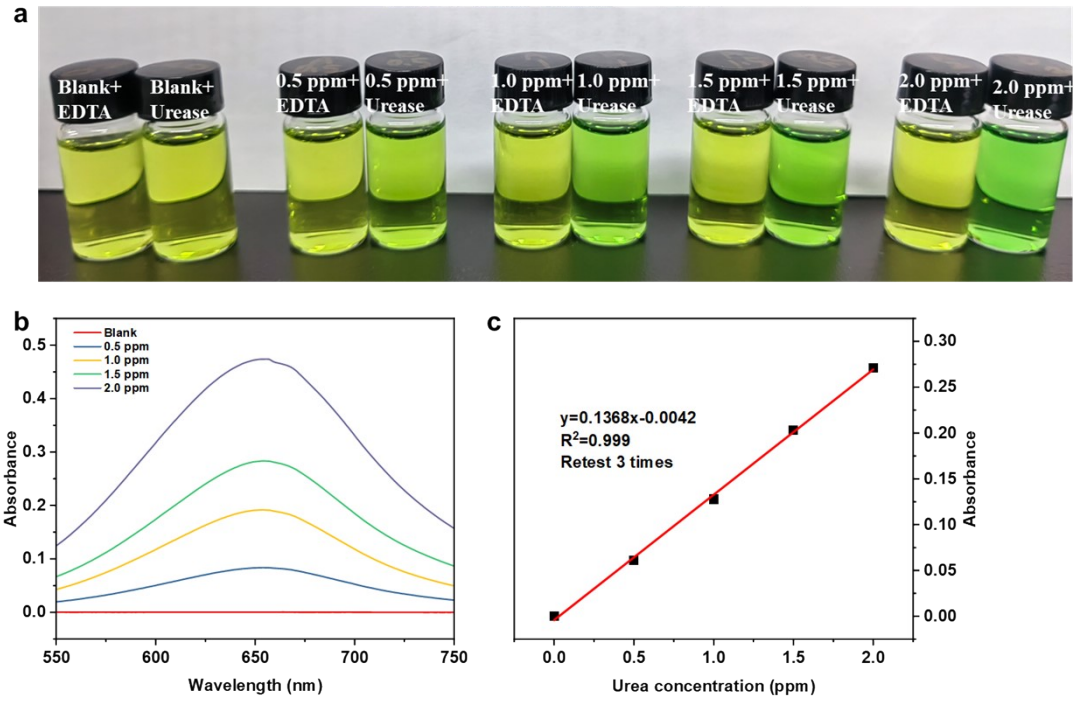

Supplementary Figure 9. Indophenol blue for urease decomposition method for urea quantification. **a,** Color of different concentration of urea quantified by urease decomposition method based on indophenol blue method, **b,** UV-vis absorption spectra of various urea concentrations, and **c,** Calibration curve used for quantifying urea.

Urea standards in **Supplementary Figure 9a** were prepared by dissolving different qualities of urea in mixed solutions of 0.1 M $KHCO_3$ and 0.05 M KNO_3.

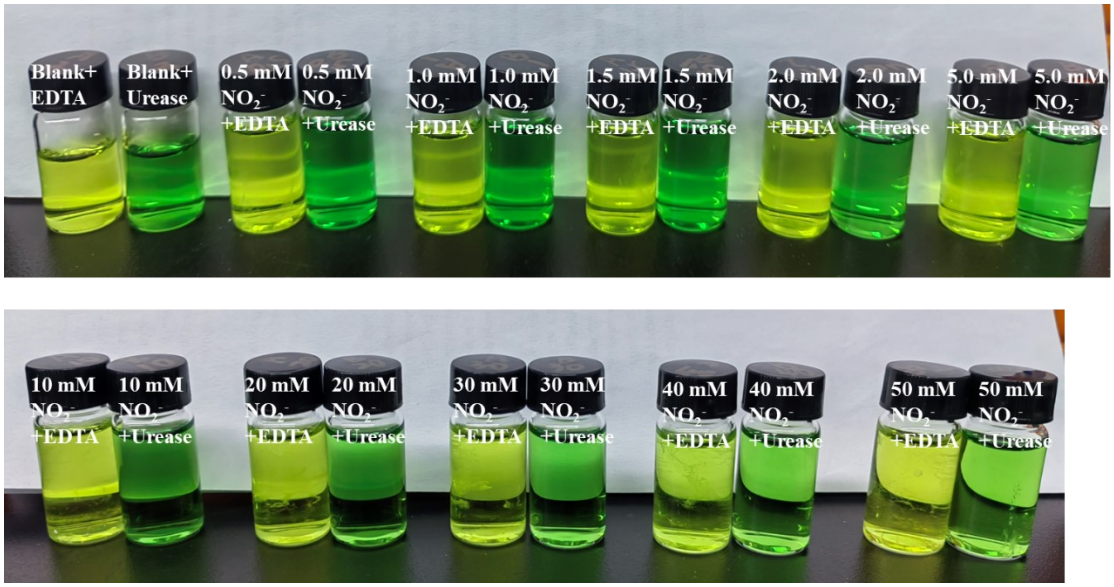

Supplementary Figure 10. Urease decomposition method for urea quantification. Color of 2.0 ppm urea with different concentration of NO_2^- quantified by urease decomposition method.

Different concentrations of NO_2^- solutions with 2.0 ppm urea were prepared and quantitatively analyzed by urease decomposition method. The samples without urease are all yellow after indophenol blue method coloration, indicates that there is no ammonia contamination in standard solutions (**Supplementary Figure 10**). Urease decomposes urea to produce ammonia, so the samples with urease added are all green, and different concentration of NO_2^- has no effect on color development. Therefore, urea quantification by urease decomposition method is not affected by coexistence of NO_2^-.

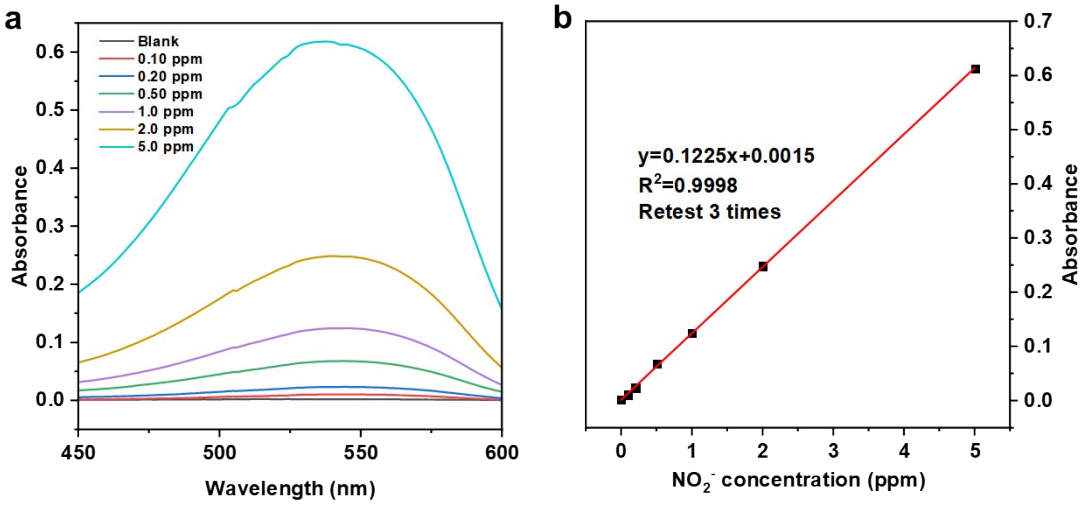

Supplementary Figure 11. Absolute calibration of the NO_2^--N detection method using KNO_2 solutions (0.1 M $KHCO_3$+0.05 M KNO_3) of known concentration as standards. **a,** UV-Vis absorption spectra of various NO_2^- concentrations, and **b,** calibration curve used for estimating NO_2^-.

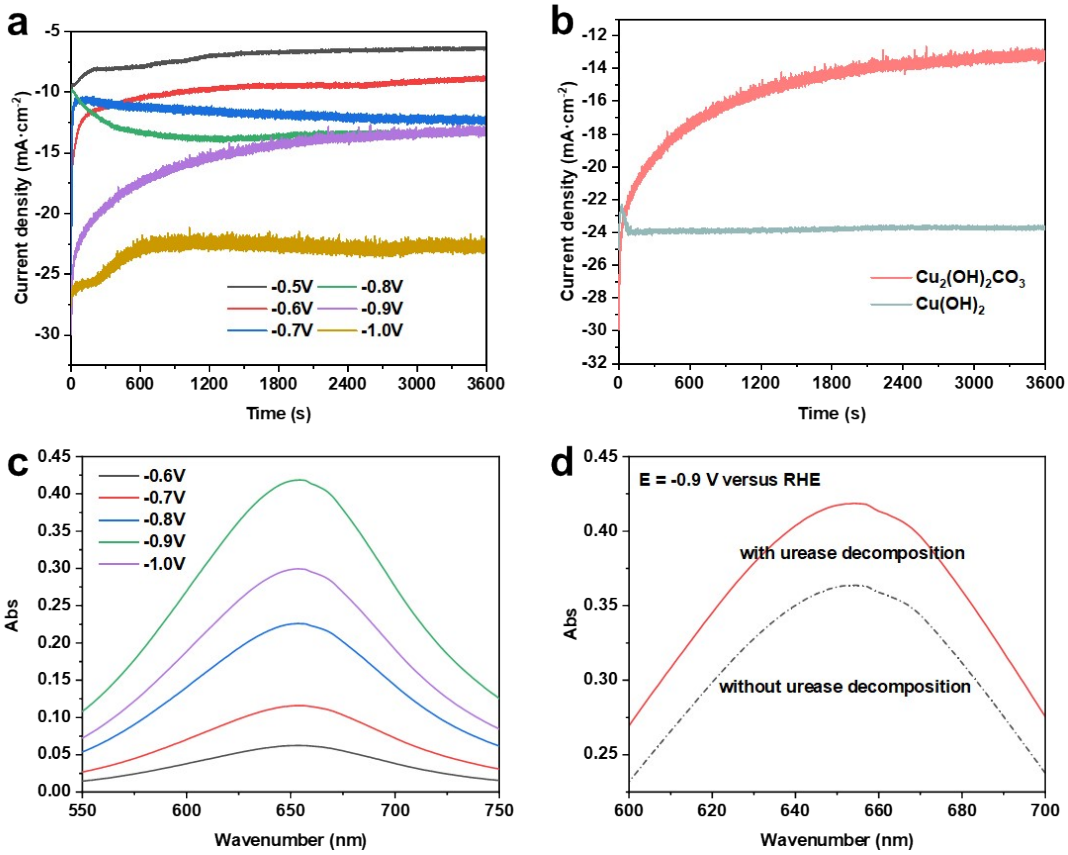

Supplementary Figure 12. a, I-t curves for electrocatalytic urea synthesis at various applied potential on $Cu_2(OH)_2CO_3$, **b,** I-t curves for electrocatalytic urea synthesis at E=-0.9V (versus RHE) on $Cu_2(OH)_2CO_3$ and $Cu(OH)_2$, **c,** UV-Vis spectra of the electrolyte of $Cu_2(OH)_2CO_3$ after charging at different potentials for 1 h with CO_2 by using indophenol blue method, and **d,** UV-vis spectra of NH_4^+ with or without urea decomposition for $Cu_2(OH)_2CO_3$ at applied potential of -0.9 V (versus RHE). The above UV-Vis curves were measured by the chromogenic solutions after 20 times dilution.

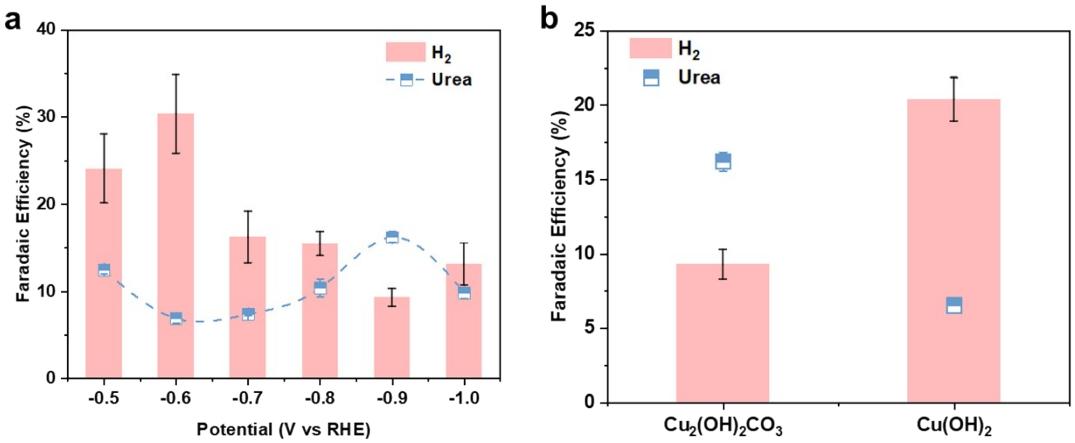

Supplementary Figure 13. Relationship of Faradaic Efficiency between urea and H_2 with **a,** various potentials, and **b,** different catalysts.

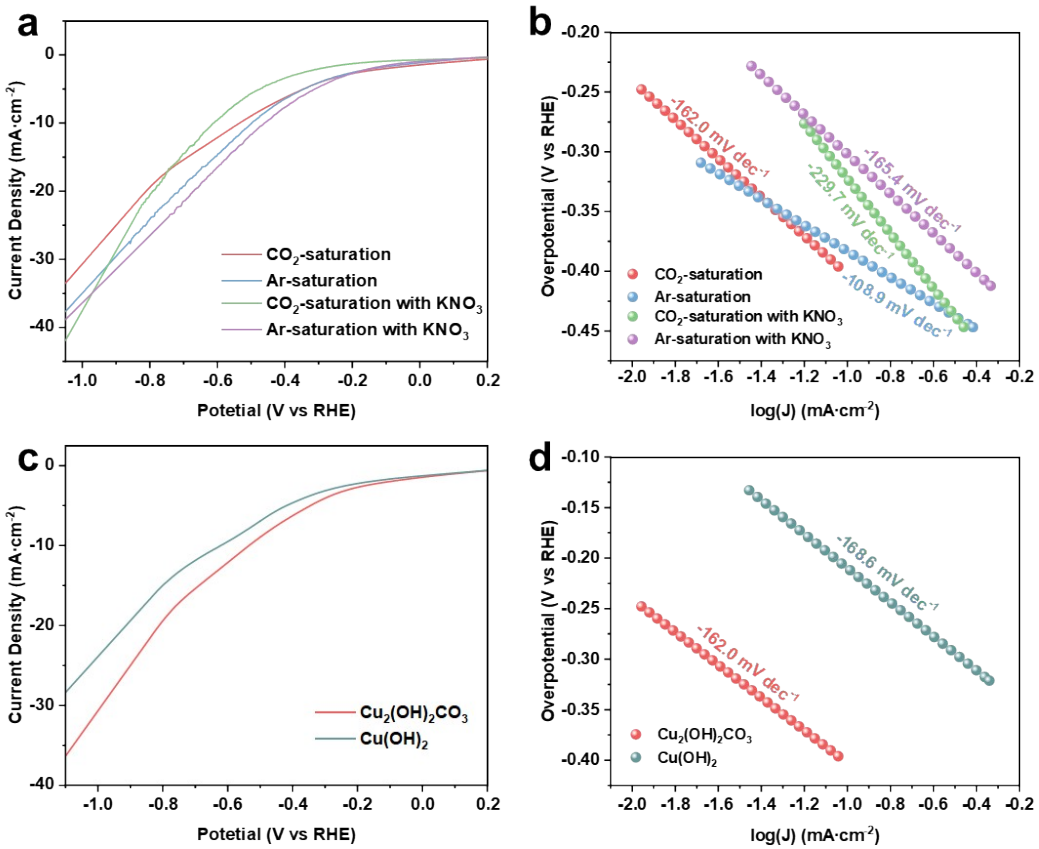

Supplementary Figure 14. a, LSV, and **b,** corresponding Tafel curves over $Cu_2(OH)_2CO_3$ with different conditions, **c,** LSV, and **d,** corresponding Tafel curves over $Cu_2(OH)_2CO_3$ and $Cu(OH)_2$ with CO_2-saturation 0.1 M $KHCO_3$+0.05 M KNO_3.

The Tafel slope is used to express the relationship between the overpotential and the logarithm of the current density, which is used to characterize the reaction rate and is closely related to the intrinsic properties of the electrocatalyst.[8, 9] As shown in Supplementary Figure 14a,b, when saturated with Ar, and the current density obtained at the same potential is smaller, the hydrogen evolution reaction is more intense. For CO_2 saturated with different electrolytes, the Tafel slope was greater for 0.1 M $KHCO_3$ + 0.05 M KNO_3 compared to 0.15 M KNO_3 alone, indicating that the presence of the $KHCO_3$ may suppress the hydrogen evolution reaction to some extent.

When comparing the LSV and Tafel curves of the two catalysts at CO_2-saturation with 0.1 M $KHCO_3$ + 0.05 M KNO_3, the $Cu_2(OH)_2CO_3$ has a smaller Tafel slope than $Cu(OH)_2$, indicating that the smaller overpotential required to provide the same increment of current density, and the faster the electron transport rate (Supplementary Figure 14c, d). High-performance electrocatalysts should have smaller Tafel slope values.

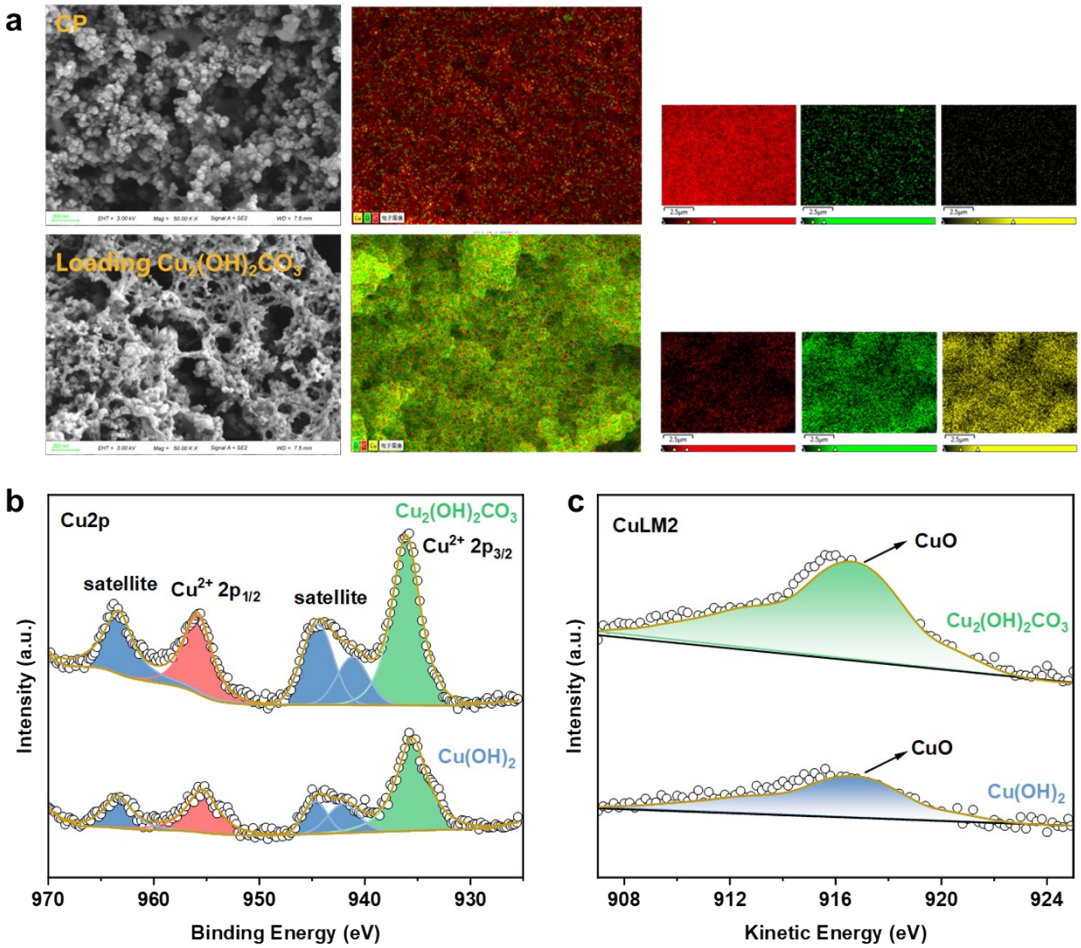

Supplementary Figure 15. a, SEM and corresponding EDS images of before and after electrode loaded $Cu_2(OH)_2CO_3$, and **b,** High resolution Cu 2p, and **c,** corresponding CuLM2 spectrums of electrodes loaded with $Cu_2(OH)_2CO_3$ and $Cu(OH)_2$.

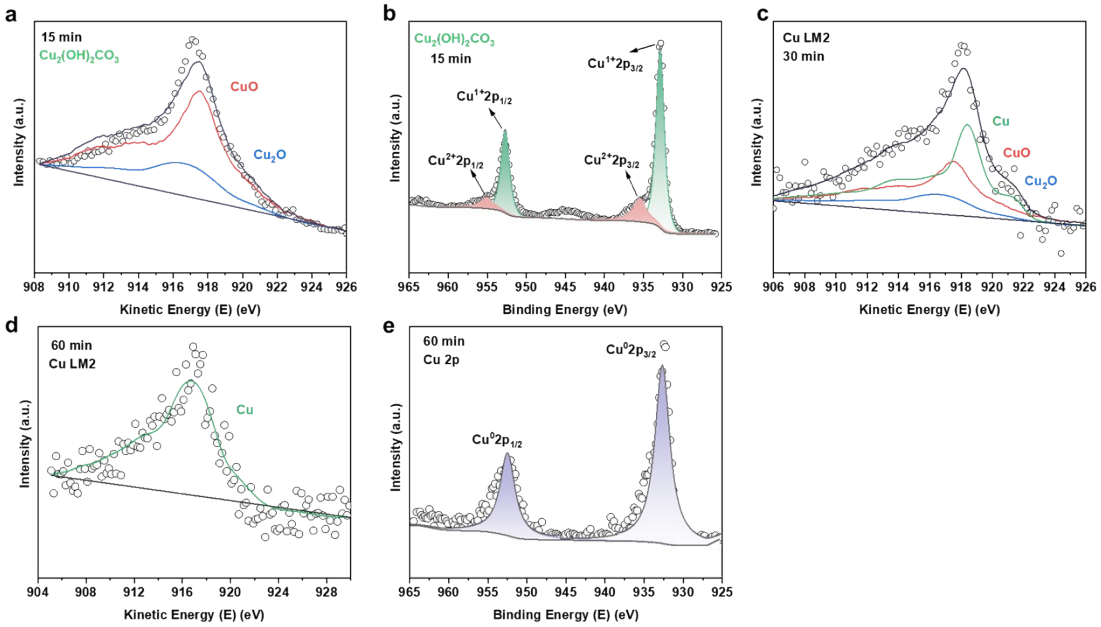

Supplementary Figure 16. a, Cu LM2, and **b,** Cu 2p spectrums of the electrode at 15 min of reaction, c, **d,** Cu LM2 spectrums of the electrode at 30 min of reaction. Cu LM2, and **e,** Cu 2p spectrums of the electrode at 60 min of reaction. The electrode is loaded with $Cu_2(OH)_2CO_3$.

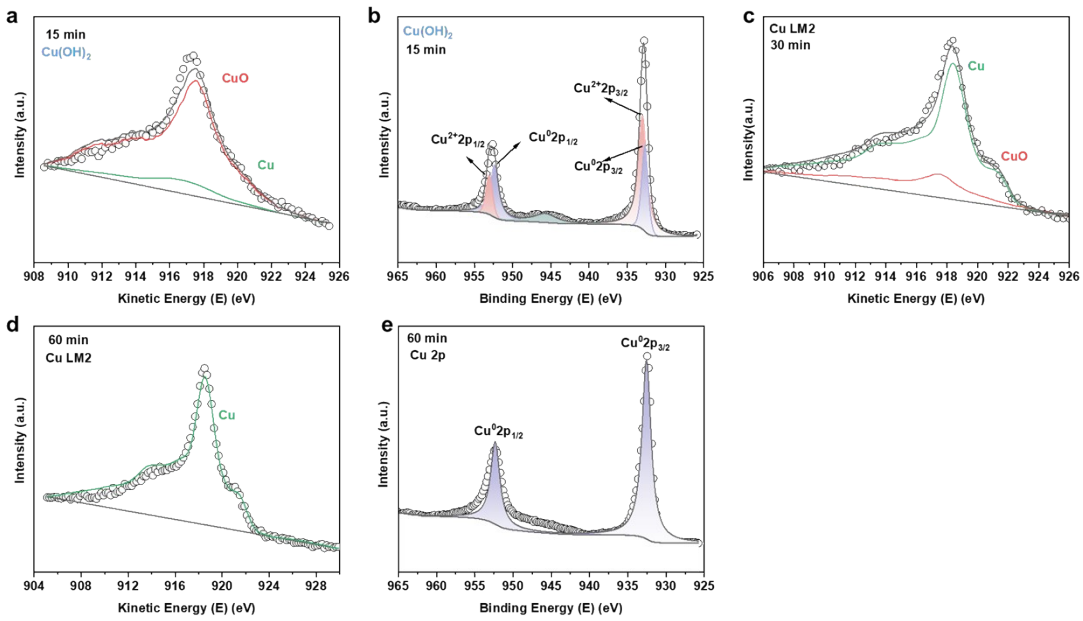

Supplementary Figure 17. a, Cu LM2, and **b,** Cu 2p spectrums of the electrode at 15 min of reaction, c, **d,** Cu LM2 spectrums of the electrode at 30 min of reaction. Cu LM2, and **e,** Cu 2p spectrums of the electrode at 60 min of reaction. The electrode is loaded with $Cu(OH)_2$.

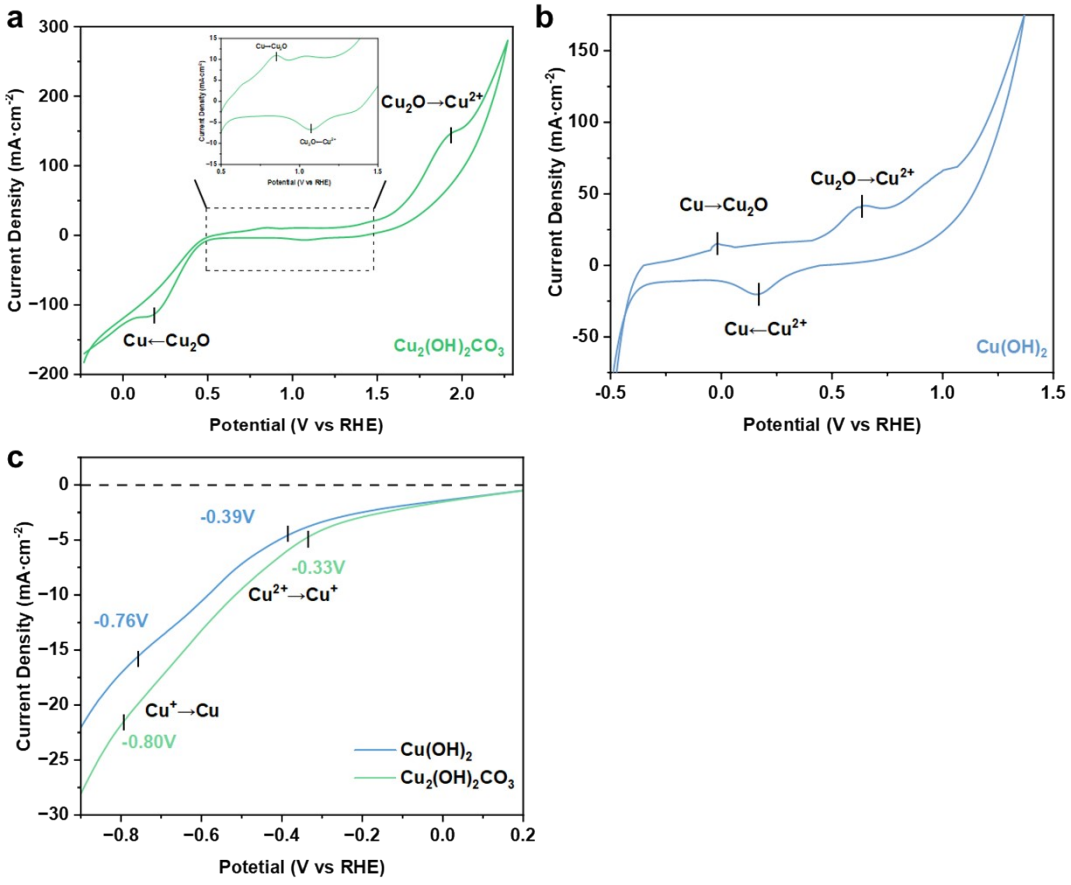

Supplementary Figure 18. Cyclic Voltammetry of **a,** $Cu_2(OH)_2CO_3$, **b,** $Cu(OH)_2$ in 0.1 M KOH, and **c,** Linear Sweep Voltammetry (LSV) with these two catalysts in Ar-saturated 0.1 M $KHCO_3$+0.05 M KNO_3. Potential sweep rate was 5 mV s^{-1}.

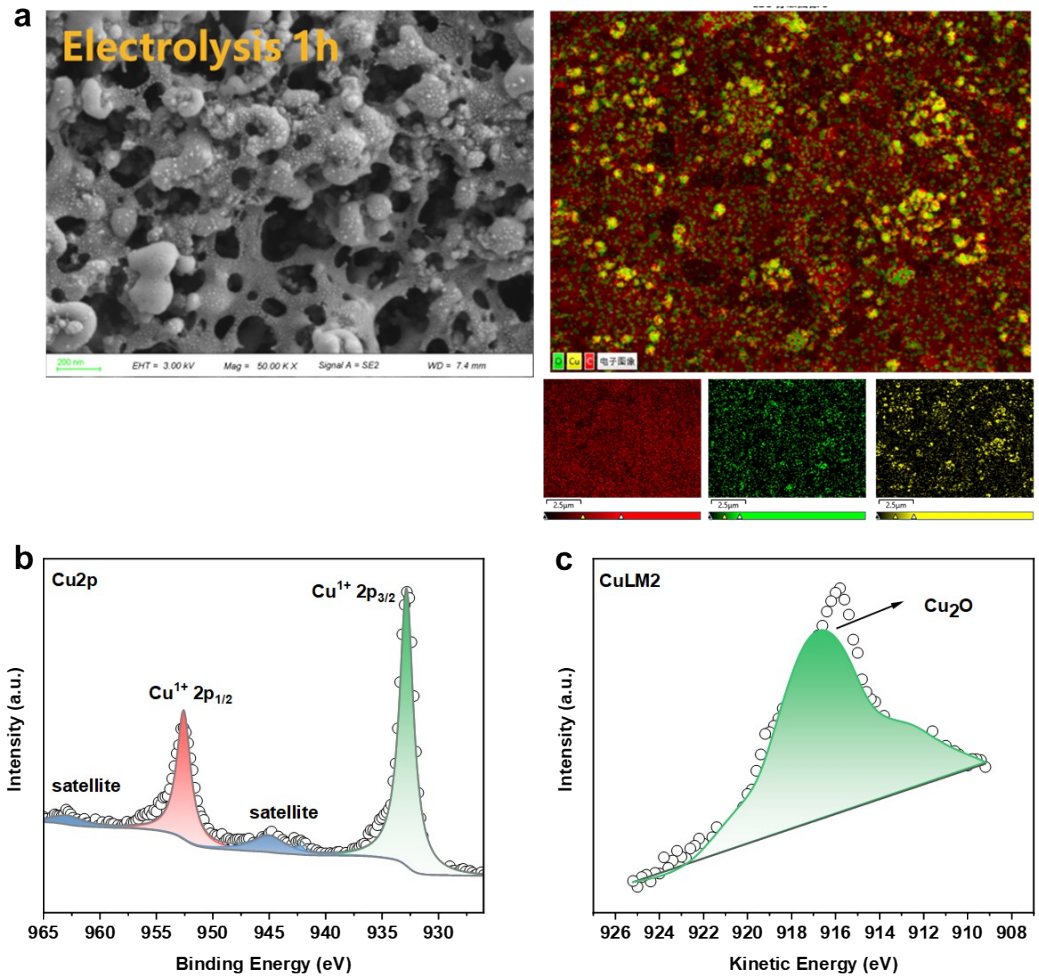

Supplementary Figure 19. a, SEM and corresponding EDS images, **b,** High resolution Cu 2p, and **c,** corresponding CuLM2 spectrums of loaded $Cu_2(OH)_2CO_3$ electrode after 1h of electrolysis.

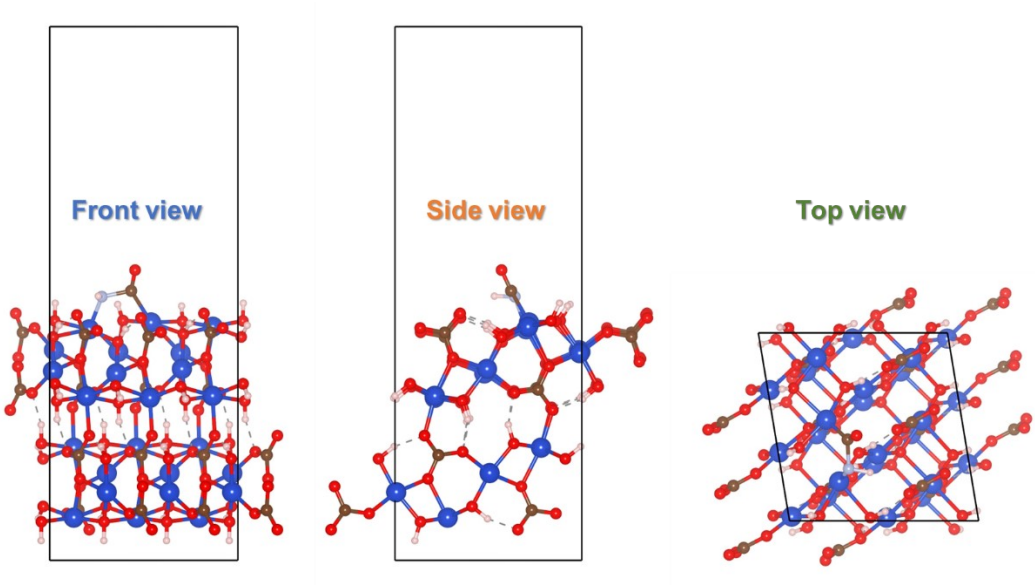

Supplementary Figure 20. The construction of $Cu_2(OH)_2CO_3$ (010) surface with different viewing angles. Red, blue, brown and pink balls represent O, Cu, C and H, respectively.

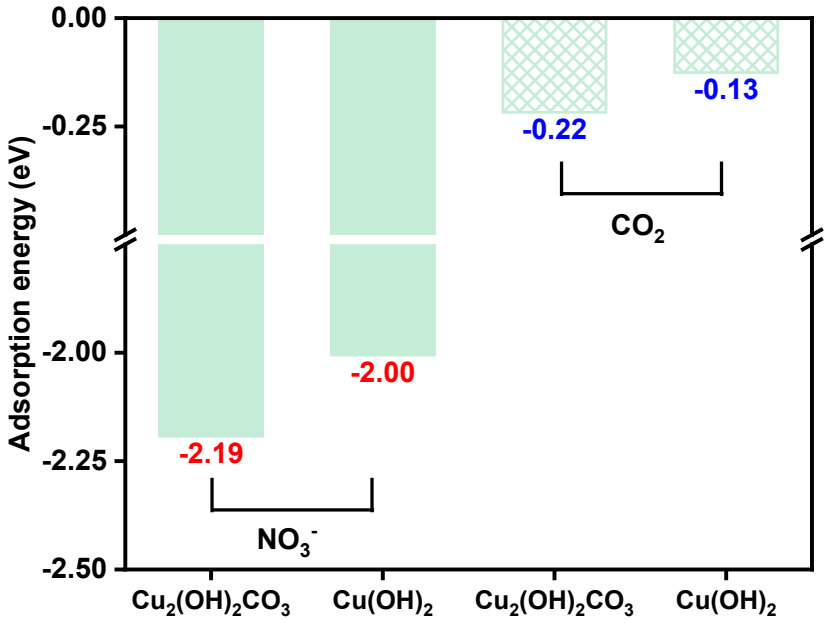

Supplementary Figure 21. Adsorption energy of NO_3^- and CO_2 on $Cu_2(OH)_2CO_3$ electrocatalysts.

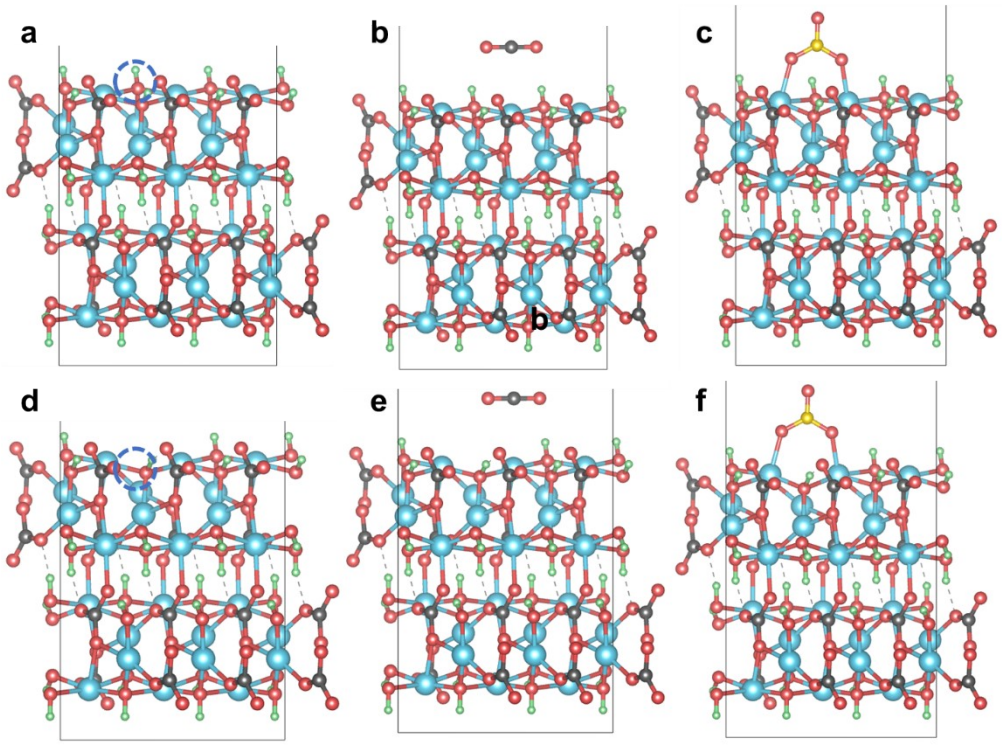

Supplementary Figure 22. Optimized adsorption configurations of CO_2 and NO_3^- on pristine and oxygen-vacancy-containing $Cu_2(OH)_2CO_3$ surfaces. a, Pristine $Cu_2(OH)_2CO_3$ surface. b, CO_2 and c, NO_3^- adsorption on pristine $Cu_2(OH)_2CO_3$. d, Oxygen-vacancy-containing $Cu_2(OH)_2CO_3$ surface, where the surface oxygen vacancy is highlighted by the dashed blue circle. e, CO_2 and f, NO_3^- adsorption on the oxygen-vacancy-containing $Cu_2(OH)_2CO_3$ surface.

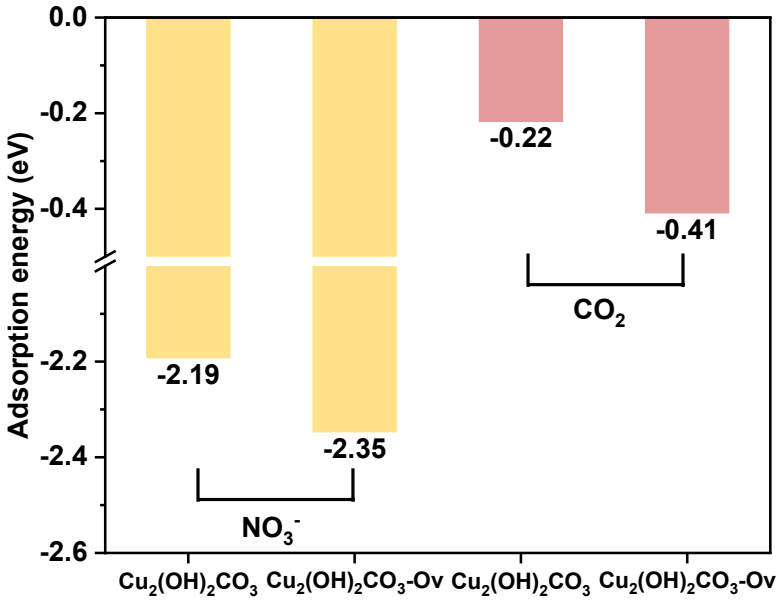

Supplementary Figure 23. Adsorption energy of NO_3^- and CO_2 on $Cu_2(OH)_2CO_3$ and oxygen-vacancy-containing $Cu_2(OH)_2CO_3$ electrocatalysts.

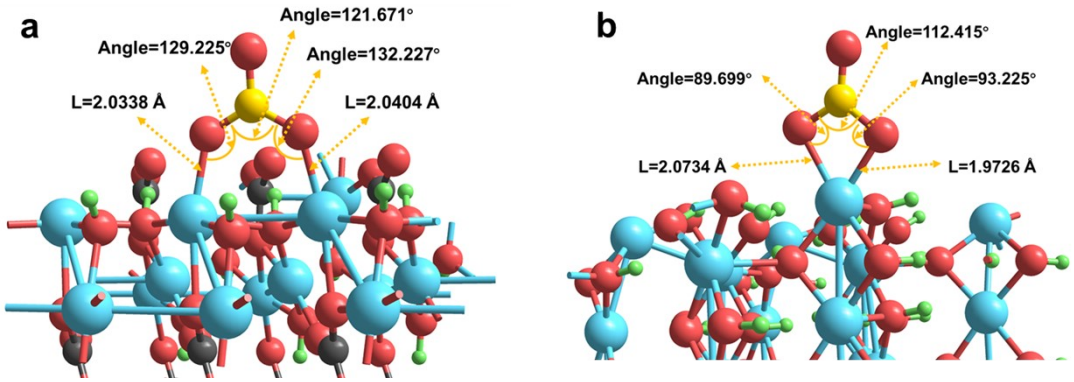

Supplementary Figure 24. Adsorption models of NO_3^- on **a,** $Cu_2(OH)_2CO_3$ and **b,** $Cu(OH)_2$ electrocatalysts. The bond length and bond angle changes when nitrate is adsorbed on different catalyst surfaces are shown in the figures.

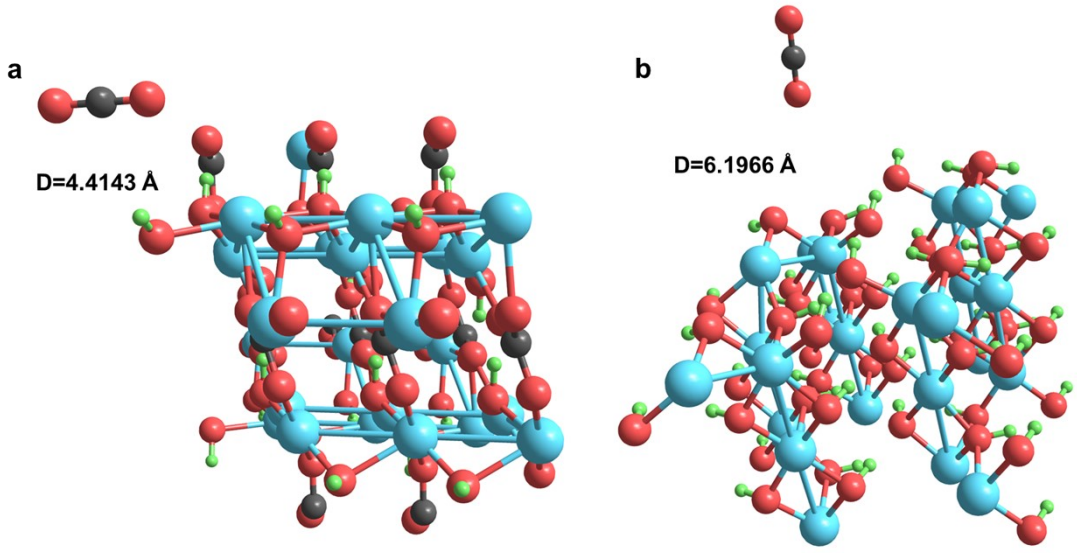

Supplementary Figure 25. Adsorption models of CO_2 on **a,** $Cu_2(OH)_2CO_3$ and **b,** $Cu(OH)_2$ electrocatalysts. The distance between the C atom in CO_2 and the Cu atom closest to the catalyst surfaces are shown in the figures.

Supplementary Table 1. Actual food waste anaerobic digestion effluent composition

Components	**Concentration**
pH	8.20±0.04
Total Solids (%)	2.09±0.04
Volatile Solids (%)	1.38±0.02
Proteins (mg/L)	1918.17±37.50
Chemical Oxygen Demand (mg/L)	63.57±0.96
PO_4^{3-} (mg/L)	15.26±0.96
NO_3^--N (mg/L)	269.54±2.71
NO_2^--N (mg/L)	5.10±0.05
NH_4^+-N (mg/L)	3558.36±50.74

The anaerobic digestion effluent was obtained after 30 days of anaerobic digestion of food waste collected from a university canteen. Its main components are shown in **Supplementary Table 1**. Where total solids (TS) is the total amount of all solids (dissolved and suspended solids) in the liquid. And the volatile solids (VS) refers to the portion of solids that is volatilized/burned off under high temperature scorching, which usually represents the organic content. The anaerobic digestion effluent was filtered through a 0.22 μm membrane to remove solid impurities before the electrocatalytic reaction. Due to the high nutrient content of food waste, the post-digestion effluent contained elevated concentrations of soluble proteins and PO_4^{3-} arising from protein hydrolysis. As for Chemical Oxygen Demand (COD), it's the amount of oxygen consumed by all organic and some inorganic substances that can be oxidized in the liquid under strong oxidant and acidic conditions, reflecting the overall oxidizable load. It is worth noting that digestion effluent contains significant amounts of NH_4^+-N, low concentrations of NO_3^--N, and virtually nonexistent NO_2^--N, and these different forms of nitrogen provide a potential source for electrocatalytic C–N coupling for urea production.

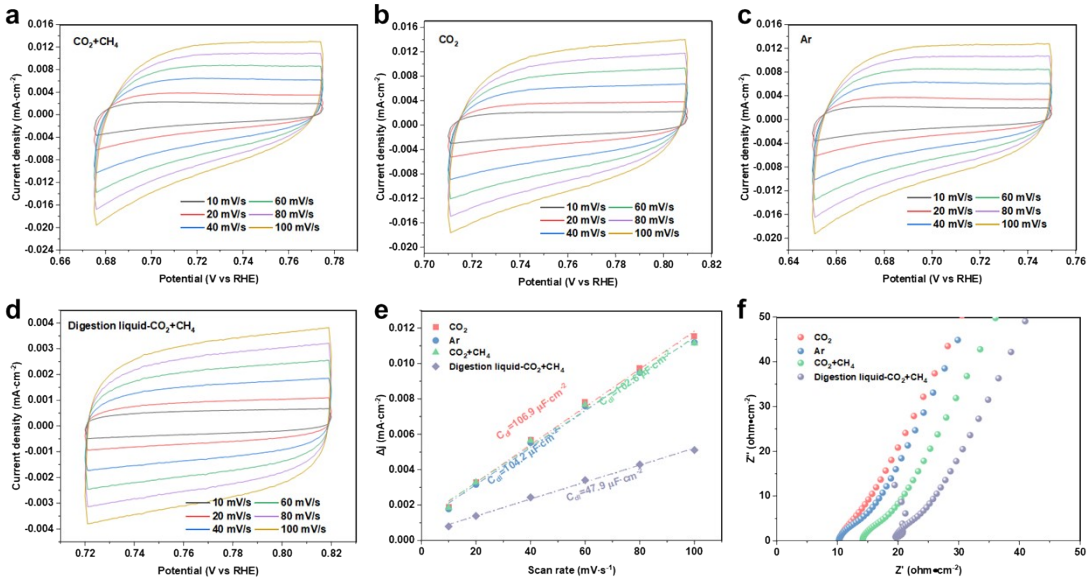

Supplementary Figure 26. The electrochemical active surface area measurements under different conditions. Cyclic voltammogram curves of **a,** 30% CO_2+70% CH_4-, **b,** CO_2-, **c,** Ar-saturated 0.2M NH_4HCO_3+0.005M KNO_3, and **d,** 30% CO_2+70% CH_4-saturated real digestion effluent. **e,** Cdl, and **f,** Nyquist curves of corresponding conditions.

As shown in **Supplementary Figure 26**, In the simulated food waste anaerobic digestion effluent, the ECSA and resistance of the electrodes did not differ much when saturated with different gases. In contrast, when using the actual anaerobic digestion effluent, the ECSA of the electrode decreases significantly and the solution internal resistance and electrode resistance increase.

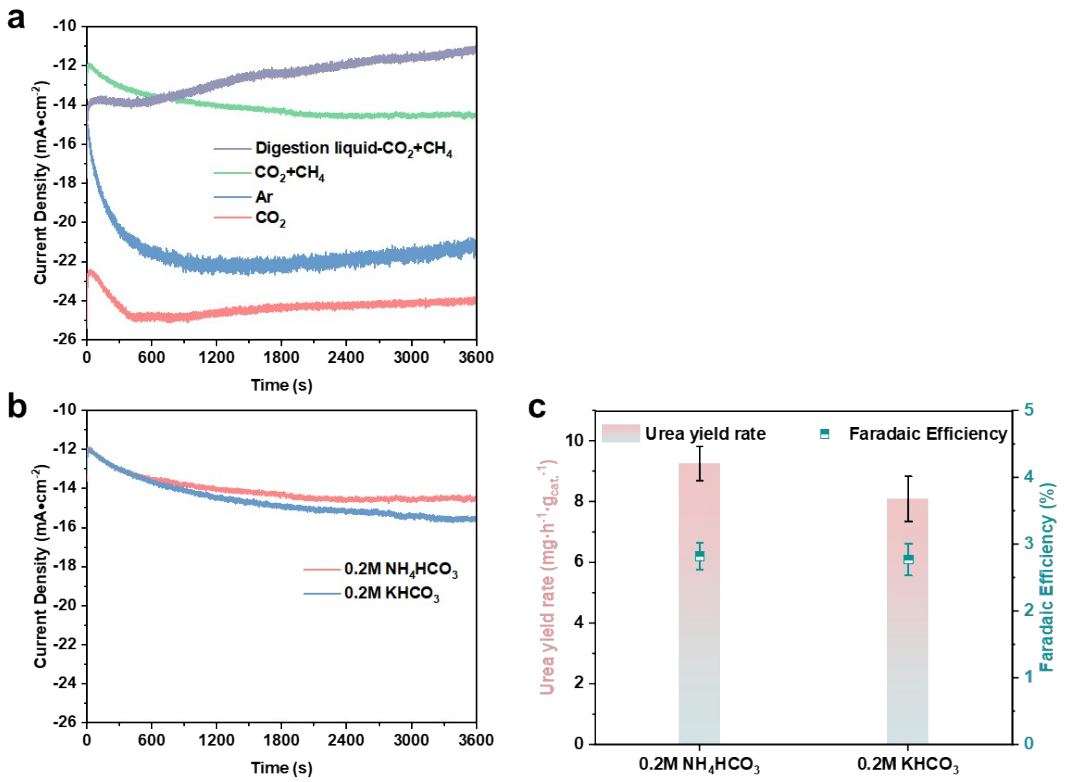

Supplementary Figure 27. I-t curves of different **a,** conditions and **b,** coexisting electrolyte at −0.9V vs RHE. **c,** Yield rate of urea and corresponding FE with different electrolyte at −0.9V vs RHE.

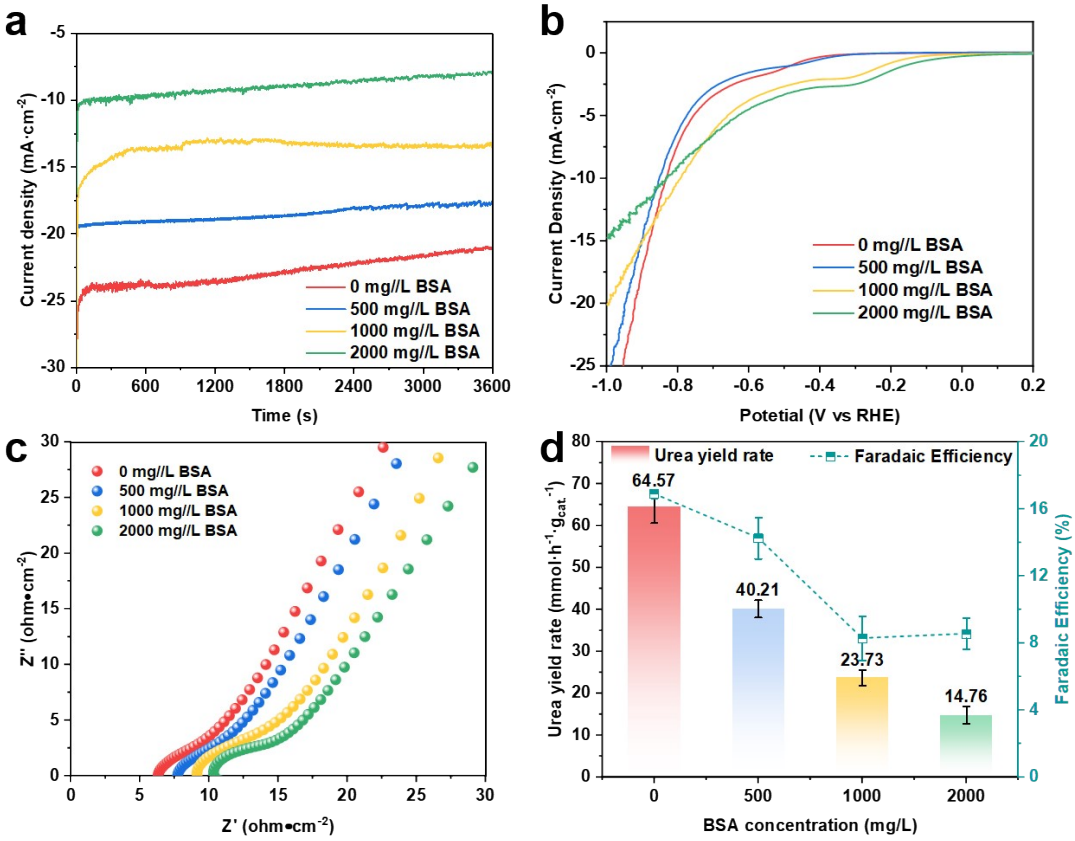

Supplementary Figure 28. Effect of BSA concentration on electrocatalytic urea synthesis over $Cu_2(OH)_2CO_3$. a, I-t curves, b, LSV curves, c, Nyquist plots and d, Urea yield rate and Faradaic efficiency under different BSA concentrations.

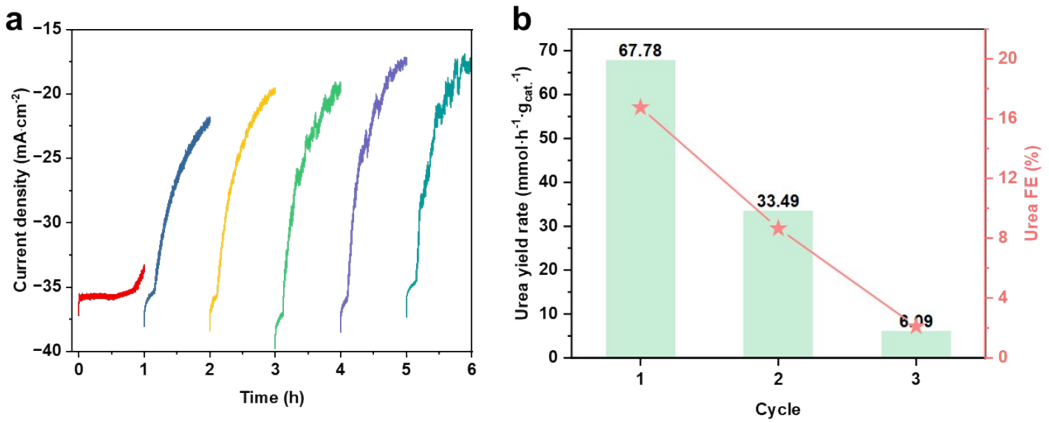

Supplementary Figure 29. a, I-t curves of $Cu_2(OH)_2CO_3$ during 5 h electrocatalytic urea synthesis at −0.9 V versus RHE in CO_2-saturated 0.1 M $KHCO_3$ + 0.05 M KNO_3. b, Changes in urea yield rate and selectivity during the first 3 cycles of $Cu_2(OH)_2CO_3$ electrocatalysis.

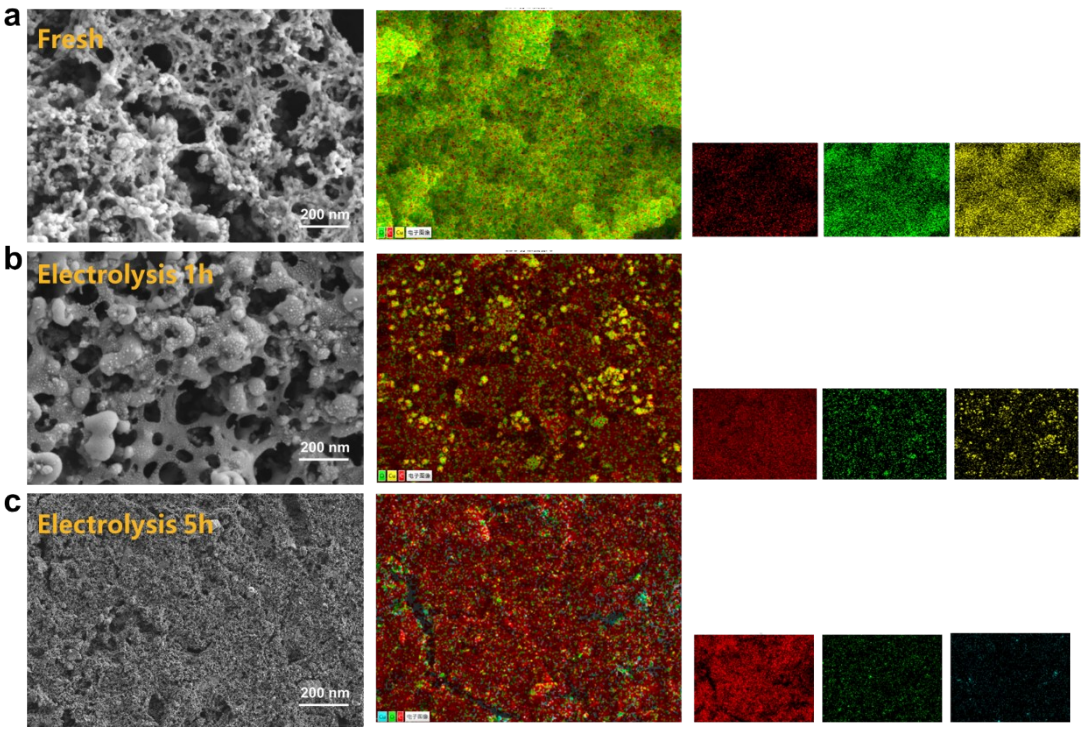

Supplementary Figure 30. SEM images and corresponding EDS elemental mappings of $Cu_2(OH)_2CO_3$ a, electrodes before electrolysis, b, after 1 h electrolysis, and c, after 5 h electrolysis.

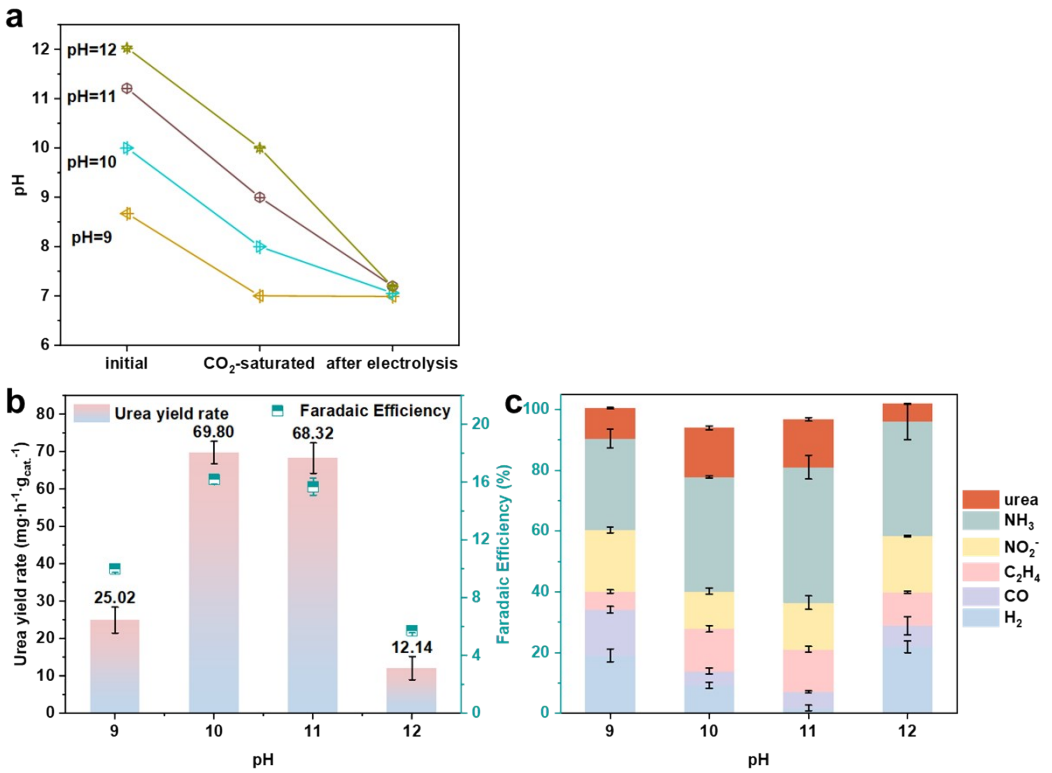

Supplementary Figure 31. a, pH evolution of electrolytes with different initial pH values after CO_2 saturation for 30 min and after 1 h electrolysis. b, Urea yield rate and Faradaic efficiency and c, Product distribution of $Cu_2(OH)_2CO_3$ at different initial electrolyte pH values at -0.9 V versus RHE. The electrolyte consists of 0.1 M $KHCO_3$ and 0.05 M KNO_3 and the pH is adjusted with 2 M KOH.

Supplementary References

1. G. Kresse and J. Furthmüller, Phys Rev B Condens Matter, 1996, 54, 11169-11186.
2. G. Kresse and D. Joubert, Physical Review B, 1999, 59, 1758-1775.
3. J. P. Perdew, K. Burke and M. Ernzerhof, Physical Review Letters, 1996, 77, 3865-3868.
4. S. Grimme, J. Antony, S. Ehrlich and H. Krieg, The Journal of Chemical Physics, 2010, 132.
5. H. J. Monkhorst and J. D. Pack, Physical Review B, 1976, 13, 5188-5192.
6. C. Wei, S. Sun, D. Mandler, X. Wang, S. Z. Qiao and Z. J. Xu, Chemical Society Reviews, 2019, 48, 2518-2534.
7. K. A. Stoerzinger, M. Risch, B. Han and Y. Shao-Horn, ACS Catalysis, 2015, 5, 6021-6031.
8. H. Xiao, T. Cheng and W. A. Goddard, III, Journal of the American Chemical Society, 2017, 139, 130-136.
9. A. M. Limaye, J. S. Zeng, A. P. Willard and K. Manthiram, Nature Communications, 2021, 12, 703.